Relating Convective and Stratiform Rain to Latent Heating

WEI-KUO TAO

Laboratory for Atmospheres, NASA Goddard Space Flight Center, Greenbelt, Maryland

STEPHEN LANG

Laboratory for Atmospheres, NASA Goddard Space Flight Center, Greenbelt, and Science Systems and Applications, Inc., Lanham, Maryland

XIPING ZENG

Laboratory for Atmospheres, NASA Goddard Space Flight Center, Greenbelt, and Goddard Earth Sciences and Technology Center, University of Maryland, Baltimore County, Baltimore, Maryland

SHOICHI SHIGE

Graduate School of Science, Kyoto University, Kyoto, Japan

YUKARI TAKAYABU

Center for Climate System Research, University of Tokyo, Tokyo, Japan

(Manuscript received 5 June 2009, in final form 23 October 2009)

ABSTRACT

The relationship among surface rainfall, its intensity, and its associated stratiform amount is established by examining observed precipitation data from the Tropical Rainfall Measuring Mission (TRMM) Precipitation Radar (PR). The results show that for moderate–high stratiform fractions, rain probabilities are strongly skewed toward light rain intensities. For convective-type rain, the peak probability of occurrence shifts to higher intensities but is still significantly skewed toward weaker rain rates. The main differences between the distributions for oceanic and continental rain are for heavily convective rain. The peak occurrence, as well as the tail of the distribution containing the extreme events, is shifted to higher intensities for continental rain. For rainy areas sampled at 0.5° horizontal resolution, the occurrence of conditional rain rates over 100 mm day^{-1} is significantly higher over land. Distributions of rain intensity versus stratiform fraction for simulated precipitation data obtained from cloud-resolving model (CRM) simulations are quite similar to those from the satellite, providing a basis for mapping simulated cloud quantities to the satellite observations.

An improved convective–stratiform heating (CSH) algorithm is developed based on two sources of information: gridded rainfall quantities (i.e., the conditional intensity and the stratiform fraction) observed from the TRMM PR and synthetic cloud process data (i.e., latent heating, eddy heat flux convergence, and radiative heating/cooling) obtained from CRM simulations of convective cloud systems. The new CSH algorithm-derived heating has a noticeably different heating structure over both ocean and land regions compared to the previous CSH algorithm. Major differences between the new and old algorithms include a significant increase in the amount of low- and midlevel heating, a downward emphasis in the level of maximum cloud heating by about 1 km, and a larger variance between land and ocean in the new CSH algorithm.

Corresponding author address: Dr. W.-K. Tao, Laboratory for Atmospheres, NASA GSFC, Greenbelt, MD 20771.
E-mail: wei-kuo.tao-1@nasa.gov

DOI: 10.1175/2009JCLI3278.1

1. Introduction

The release of latent heating (LH) during the formation of precipitation is of immense consequence to the nature of large- and small-scale atmospheric circulations, particularly in the tropics where various large-scale tropical modes controlled by LH persist and vary on a global scale. Latent heat release and its variations are without doubt the most important diabatic processes within the atmosphere, and thus play a central role in the earth's water cycle. Latent heating is dominated by phase changes between water vapor and small liquid or frozen cloud-sized particles. It consists of the condensation of cloud droplets, evaporation of cloud droplets and raindrops, freezing of cloud droplets and raindrops, melting of snow and graupel/hail, and the deposition and sublimation of ice particles. In addition, eddy heat flux convergence from cloud motions can also redistribute the heating or cooling vertically and horizontally. LH cannot be measured directly with current techniques, including current remote sensing or in situ instruments, which explains why nearly all retrieval schemes depend heavily on some type of cloud-resolving model (CRM). However, apparent heating or Q_1, of which LH is an important component, can be derived indirectly by measuring vertical profiles of temperature and the associated 3D wind fields from extensive rawinsonde networks through a residual method (known as a diagnostic heating budget; Yanai et al. 1973).

The launch of the Tropical Rainfall Measuring Mission (TRMM) satellite, a joint U.S.–Japan project, in November 1997 made it possible for quantitative measurements of tropical rainfall to be obtained on a continuous basis over the entire global tropics. TRMM provides a much-needed accurate measurement of rainfall as well as an estimate of the four-dimensional structure of LH (or diabatic heating) over the global tropics. Over the last few years, standard LH products from TRMM measurements have become established as a valuable resource for scientific research and applications (see a review by Tao et al. 2006). Such products enable new insights and investigations into the complexities of convective system life cycles, diabatic heating controls and feedbacks related to mesoscale to synoptic-scale circulations and their forecasting, the relationship of tropical patterns of LH to the global circulation and climate, and strategies for improving cloud parameterizations in environmental prediction models.

Five different TRMM LH algorithms designed to use satellite-estimated surface rain rates and precipitation profiles have been developed, intercompared, validated, and applied in the past decade (see Tao et al. 2006, 2007). They are the Goddard convective–stratiform heating (CSH) algorithm, the hydrometeor heating (HH) algorithm, the Goddard profiling heating (GPROF heating) algorithm,[1] the spectral latent heating (SLH) algorithm, and the precipitation radar heating (PRH) algorithm. The CSH algorithm only requires information on the surface precipitation rates, amount of stratiform rain, and the type and location of the observed cloud systems[2] (Tao et al. 1993a). A lookup table (LUT), however, is used, which contains stored mean diabatic convective and stratiform heating profiles that have been normalized respectively by their mean convective and stratiform surface rain rates for various types of cloud systems in different geographic locations. These profiles are mostly obtained from CRM [i.e., the Goddard Cumulus Ensemble (GCE) model] simulations but also include profiles from sounding budget studies. In GPROF, CRM-simulated vertical profiles of hydrometeors (and associated LH) that have radiative characteristics consistent with a given set of multispectral microwave radiometric observations are composited to create (retrieve) a best estimate of the observed profiles (Olson et al. 1999; Grecu et al. 2009). The HH algorithm[3] estimates LH profiles as a function of the vertical derivative of the retrieved hydrometeor profiles (Yang and Smith 1999). The derivation and evaluation of the HH algorithm is also based on CRM simulations. It requires information about the vertical profiles of cloud- and precipitation-sized water and ice particles, all of which can be obtained from passive microwave measurements, including those from the TRMM Microwave Imager (TMI; Smith et al. 1994). The terminal (fall) velocities of the large cloud (precipitating) particles (rain, snow, and graupel/hail) are also required for the HH algorithm, as is the cloud-scale velocity, which is obtained by applying a regression method to a CRM-simulated database. The SLH algorithm (Shige et al. 2004, 2007, 2008, 2009) is also based on CRM (i.e., GCE) results. It uses TRMM Precipitation Radar (PR) information (i.e., melting layer, precipitation top height, rain rate and type) to select the heating profiles from a LUT. The PRH algorithm (Satoh and Noda 2001; M. Katsumata et al. 2008, unpublished manuscript) also uses PR information but without using any CRM-simulated heating profiles. However, it needs to estimate the cloud drafts and (standard) thermodynamic structures associated with cloud systems. An iteration calculation is

[1] The GPROF heating algorithm was recently replaced by the TRAIN algorithm.

[2] The CSH algorithm regularly uses PR echo top heights to include shallow convection.

[3] Tao et al. (1990) were the first to put forth a LH algorithm that was termed a hydrometeor heating algorithm. Tao et al. (1993a) then improved the performance of their HH algorithm by including surface rain rates.

TABLE 1. Summary of the five LH algorithms participating. Data inputs, retrieved products, and salient references included. Note that the conventional relationship between Q_1 (apparent heat source), LH, and Q_R (radiative heating) is expressed by $Q_1 - Q_R = \text{LH} + \text{EHT}$, where the final term represents eddy heat transport by clouds (noting that vertically integrated EHT is zero; i.e., it provides no explicit influence on surface rainfall). Note that CSH, SLH, and TRAIN explicitly use CRM-simulated latent heating profiles in their heating algorithm lookup tables. Both HH and PRH also implicitly use CRM-simulated results (i.e., cloud vertical velocity).

	TRMM data needed	Heating products	Key references in algorithm description
CSH (Convective-stratiform heating)	PR, TMI, PR–TMI	Q_1, LH	Tao et al. (1993a, 2000, 2001)
SLH (Spectral latent heating)	PR	LH, $Q_1 - Q_R$	Shige et al. (2004, 2007, 2008, 2009)
TRAIN (Trained radiometer algorithm)	TMI (PR training)	$Q_1 - Q_R$, LH	Grecu and Olson (2006); Olson et al. (2006); Grecu et al. (2009)
HH (Hydrometeor heating)	PR–TMI	LH	Yang and Smith (1999); Yang et al. (2006)
PRH (Precipitation radar heating)	PR	LH	Satoh and Noda (2001); M. Katsumata et al. (2008, unpublished manuscript)

applied to match the relationship between rainfall and LH. The strengths and weaknesses of each algorithm were discussed in Tao et al. (2006). Table 1 lists the required data, type of heating product, and the key references for each of these algorithms.

In this paper, both TRMM PR and CRM-simulated results will be used to examine and quantify the relationship among stratiform rain fraction, surface rain intensity, and LH for convective systems of various geographic origins. The results from the GCE model simulations will be used to calculate each of the major components of the atmospheric heating budget (i.e., LH, eddy transport, and radiation). These simulated results are then used to develop a new CSH algorithm. In section 2, the model, its setup, and the cases are described. The results are shown and discussed in section 3. In section 4, the performance of the new CSH algorithm is presented. Finally, the major results and future work are summarized in section 5.

2. Numerical modeling and data

a. Goddard cumulus ensemble model

The GCE is a CRM and is used to simulate clouds/cloud systems and their associated heating budget. The model is nonhydrostatic. It accounts for both absorption and scattering for solar radiation and both emission and absorption for infrared radiation and has been used to study cloud–radiation interactions (Tao et al. 1996, 2003a). Subgrid-scale (turbulent) processes in the model are parameterized using a scheme based on Klemp and Wilhelmson (1978). The effects of both dry and moist processes on the generation of subgrid-scale kinetic energy have been incorporated (Soong and Ogura 1980). The sedimentation of cloud ice (Starr and Cox 1985) is included to better model clouds in the upper troposphere. All scalar variables (i.e., temperature, water vapor, and all hydrometeors) are advected with a positive definite advection scheme. Results from the positive definite advection scheme are in better agreement with observations for tropical cloud systems (Johnson et al. 2002).

The model has five prognostic hydrometeor variables: the mixing ratios of cloud water, rainwater, cloud ice, snow, and graupel. The model's bulk microphysics scheme was recently modified by Lang et al. (2007) to reduce the unrealistically large amount of precipitating ice particles (mainly graupel) in the model and by Zeng et al. (2008, 2009) to introduce the ice nuclei concentration into the parameterization of the Bergeron process as an input factor. The development and main features of the GCE model were published in Tao and Simpson (1993) and Tao et al. (2003a). A review on the application of the GCE model to better understand precipitation processes can be found in Simpson and Tao (1993) and Tao (2003).

In the GCE model, each grid point is designated as either a cloudy or clear area for each integration time, depending on whether the sum of the cloud water and ice mixing ratios are larger than 10^{-3} g kg^{-1} at each grid point (usually an indicator of 100% relative humidity). In the cloudy area, each grid point can also be designated as either being in the active or nonactive updraft or downdraft region (Tao et al. 1987). In addition, the cloud characteristics can be divided into their convective and stratiform components (Tao et al. 1991, 1993b; Lang et al. 2003). In short, convective regions include those with large vertical velocities (exceeding 3–5 m s^{-1}) and/or large surface precipitation rates. The stratiform region is separated into regions with and without surface rainfall.

The model used in this study has the same structure as that in previous studies (e.g., Soong and Tao 1980; Tao and Soong 1986; Johnson et al. 2002; Tao et al. 2003b, 2004; Zeng et al. 2007; and many others) wherein clouds

TABLE 2. Field campaigns (ARM, SCSMEX, TOGA COARE, and GATE) including the geographic location, starting time, and integration length of GCE model simulations. Also included are the previous GCE modeling papers that have simulated the case.

Field campaign	Geographic location	Starting date	Modeling days	
ARM-SGP-97	(37°N, 97°W)	18 Jun 1997	29	Tao et al. (2004); Zeng et al. (2009)
ARM-SGP-02		25 May 2002	20	Zeng et al. (2007, 2009)
SCSMEX/NESA	(21°N, 117°E)	6 May 1998	44	Tao et al. (2003b); Zeng et al. (2008)
TOGA COARE	(2°S, 154°E)	1 Nov 1992	61	Das et al. (1999); Johnson et al. (2002); Zeng et al. (2009)
GATE	(9°N, 24°W)	1 Sep 1974	18	Li et al. (2002); Zeng et al. (2009)

are simulated under prescribed large-scale forcing. The default numerical experiment is two-dimensional (2D), using a 1-km horizontal resolution and vertical resolution that ranges from 42.5 m at the bottom to 1 km at the model top, which is at 22.5 km. The model uses a time step of 6 s and 512 × 41 grid points for integration. Please see Zeng et al. (2008, 2009) for more details.

b. Data

1) OCEANIC CONVECTIVE SYSTEMS (GATE, TOGA COARE, AND SCSMEX)

The South China Sea Monsoon Experiment (SCSMEX) was conducted in May–June 1998. Two major convective events, one prior to and during monsoon onset (18–26 May 1998) and the other post monsoon onset (2–11 June 1998), were observed. The SCSMEX forcing data were obtained from a variational analysis approach (Zhang and Lin 1997; Zhang et al. 2001) and used to drive the GCE model for 44 days starting at 0600 UTC 6 May 1998. The Tropical Ocean Global Atmosphere–Coupled Ocean Atmosphere Response Experiment (TOGA COARE) was conducted in 1992/93 over the central Pacific. The most intense convection during TOGA COARE occurred in mid and late December 1992, prior to the peak in westerly wind bursts around 1 January 1993. Several major convective events occurred around 11–16 and 20–25 December 1992, mainly due to the low-level, large-scale convergence of easterlies and westerlies (Ciesielski et al. 2003). For TOGA COARE, the large-scale forcing used in the GCE model was derived from the Intensive Flux Array (IFA) sounding network (Lin and Johnson 1996). The Global Atmospheric Research Program (GARP) Atlantic Tropical Experiment (GATE) was conducted in 1974 over the east Atlantic. Cloud systems (nonsquall clusters, a squall line, and scattered convection) for the period 1–8 September 1974 during phase III of GATE have also been simulated using the GCE model (Li et al. 1999; Tao 2003). Large-scale GATE forcings from Sui and Yanai (1986) were used to drive the GCE model. The environmental conditions for SCSMEX, TOGA COARE, and GATE can be found in Tao et al. (2004). The TOGA COARE surface flux algorithm (Wang et al. 1996) is used to calculate sea surface fluxes for these oceanic cases.

2) CONTINENTAL CASES (ARM 1997 AND 2002)

The Atmospheric Radiation Measurement (ARM) program established the Southern Great Plains (SGP) site to observe clouds and precipitation for climate research. The site is centered at 36.6°N, 96.5°W. Two summer field campaigns were conducted at the site in 1997 and 2002 and are referred to here as ARM-SGP-97 and -02. The ARM forcing data were also obtained from the variational analysis approach of Zhang and Lin (1997) and Zhang et al. (2001). Surface fluxes taken from site-wide averages of observed fluxes from the ARM Energy Balance Bowen Ratio (EBBR) stations are imposed into the model (Zeng et al. 2007). The ARM-SGP-97 numerical simulation starts at 2330 UTC 18 June 1997 and lasts for 29 days. The ARM-SGP-02 simulation starts at 2030 UTC 25 May 2002 and lasts for 20 days. For the ARM cases, the surface wind does not interact with the boundary layer.

The SCSMEX, TOGA COARE, GATE, and ARM cases were all previously simulated with the GCE model. Please see Das et al. (1999), Li et al. (1999), and Zeng et al. (2009) for the GATE case; Johnson et al. (2002) and Zeng et al. (2009) for the TOGA COARE cases; Tao et al. (2003b) and Zeng et al. (2008) for the SCSMEX cases; and Xu et al. (2002) and Zeng et al. (2007, 2009) for the ARM cases regarding the temporal variation of the wind shear. Table 2 summarizes all of the GCE model integrations for these cases.

c. TRMM PR

TRMM PR data are available in a variety of forms, from raw instantaneous pixel-level data (e.g., 1B21) to processed instantaneous pixel-level data (e.g., 2A25) to a gridded monthly product containing a complete set of measurement statistics (i.e., 3A25). Although it is not limited to using rainfall data just from the PR, the original CSH algorithm (hereafter CSHv1) utilized the monthly gridded 3A25 product at 0.5° × 0.5° horizontal resolution because of the coincident measurements of echo top heights available from the PR. However, frequent

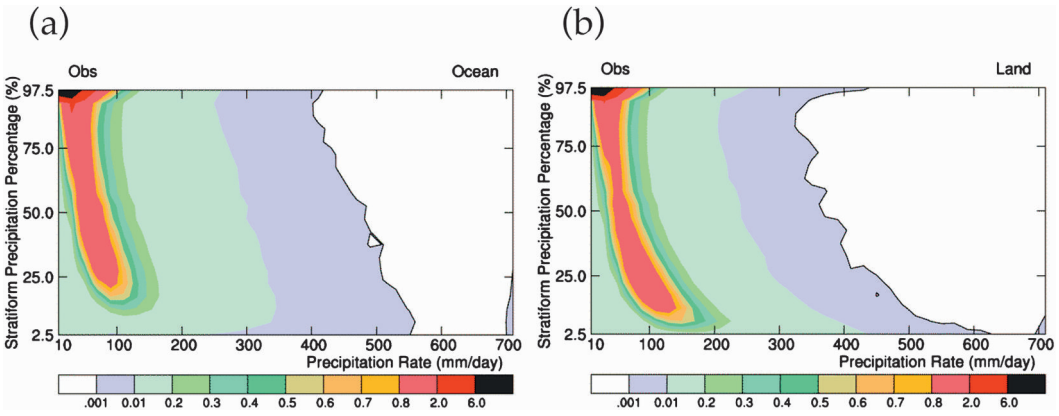

FIG. 1. Hit frequency of the TRMM observations over (a) oceanic and (b) continental regions.

demands for heating data at a higher temporal resolution to study processes on shorter time scales necessitated a change to another product: 3G68. The 3G68 product blends the convenience of a gridded product at 0.5° × 0.5° resolution with instantaneous values. It also contains rainfall data from all three TRMM rain algorithms: PR, TMI, and combined. However, it is limited strictly to surface rainfall information. By combining 3G68 with a separate dataset on PR echo top heights, CSHv1 heating profiles were generated on a daily time scale,[4] which was well received by users interested in having higher-temporal-resolution heating data. Shige et al. (2007) conducted an error analysis for the SLH algorithm and recommended that horizontal averaging over ~30 km be used for quantitative heating estimates. This makes the 3G68 gridded orbital product a suitable target for heating retrieval.

3. Results

a. *PR-estimated relationship between rain intensity and stratiform rain percentage*

Figure 1 shows the relationship between rainfall intensity and stratiform precipitation percentage for ocean and land regions based on gridded instantaneous rainfall data from the TRMM PR (i.e., 3G68). Average stratiform rain percentages and mean rain rates for rainy areas only (i.e., conditional rain rates) were computed over each 0.5° × 0.5° grid and then distributed into rain intensity and stratiform rain percentage bins of 20 mm day^{-1} and 5%, respectively. The overall pattern between the two regions is quite similar. For example, for moderate to high stratiform fractions, rain probabilities are strongly skewed toward light rain intensities (i.e., less than 100 mm day^{-1}); for convective type rain, the peak probability of occurrence and the tail of the distribution shift to higher intensities, but overall weaker rain rates still dominate the distribution in terms of occurrence. These results imply that there is a general relationship between rainfall intensity and stratiform amount, one that might be used to help formulate a retrieval algorithm. There are, however, differences in the probability distributions between oceanic and land regions. These differences are mainly in the highly convective region. For highly convective rain, both the peak occurrence and the tail of the distribution containing the extreme rainfall rates are shifted toward higher intensities for continental rain, such that for rainy areas the relative likelihood of precipitation rates over 100 mm day^{-1} is significantly higher over land. Combined with the fact that there are characteristic differences in continental versus oceanic convection, this implies that there is and should be a separation between the treatment of continental and oceanic regions.

Figure 2 shows the TRMM PR observed relationship between rainfall intensity and stratiform precipitation percentage over the SCSMEX northern enhanced sounding array (NESA) for May–June of 1998.[5] It also shows the relationship for the same SCSMEX region for 10 yr of May–June observations. Once again, the same general pattern emerges, with light rainfall dominating the probability of occurrence and peak probabilities and extreme events shifting to higher intensities for the most convective part of the distribution. The SCSMEX NESA distribution, however, appears more similar to that for land (i.e., Fig. 1b). Johnson et al. (2005) found that the stratiform rain fraction during the monsoon

[4] Although the 3G68 product contains instantaneous gridded orbital data, its effective time sampling is approximately daily when considering the TRMM satellite's coverage.

[5] Note that Ciesielski and Johnson (2006) stated that ENSO had a strong influence on the rainfall distribution over the South China Sea during SCSMEX.

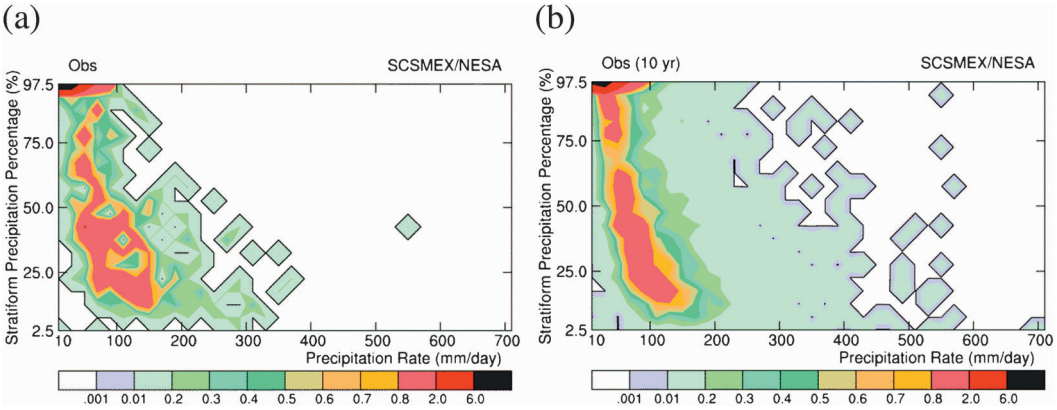

FIG. 2. (a) As in Fig. 1, but for TRMM observations over SCSMEX NESA for May–June 1998. (b) As in (a), but for 10 yr of observations.

onset in SCSMEX was relatively low. They attributed this to dry conditions aloft and relatively weak instability. In addition to rainfall amount, Table 3 shows the PR-observed mean stratiform rain percentage for the global tropics and subtropics (52.8%) and its oceanic (55.0%) and continental (47.4%) components. The stratiform fraction is about 7%–8% higher over ocean than over land. A similar relative difference is reflected in the SCSMEX versus ARM regions; however, in an absolute sense the SCSMEX region is closer to the overall land percentage. This agrees with Johnson et al.'s (2005) assessment that the stratiform fraction for SCSMEX was relatively low and explains the similarity between the SCSMEX and land stratiform fraction versus rain intensity distributions.

Schumacher and Houze (2003) examined stratiform rain in the tropics using the TRMM PR. Their results showed that stratiform rain accounted for 40% of the total rain amount from 20°N to 20°S for the 3-yr period 1998–2000. They also found that stratiform amounts were lower over land (ranging from 26% to 38%) than over ocean (ranging from 41% to 53%). For example, stratiform rain accounted for 53% of the total rainfall over the southeast Pacific but only 36% of the rain over North and South America. These findings are in good agreement with the current results in terms of land–ocean contrast. However, since the current results are based on a 10-yr period over a larger geographic area, the total stratiform rain percentage is higher in the current study because it encompasses a wider geographic domain and thus includes many more midlatitude systems (i.e., frontal), which have a higher stratiform rain percentage, especially during the cold season (e.g., Zeng et al. 2009). In addition, there are differences between the version 5 2A25 algorithm used in the Schumacher and Houze (2003) study and the version 6 PR algorithm used in this study. Convective rain rates are significantly lower in version 6.

b. *GCE model-simulated relationship between rain intensity and stratiform rain percentage*

To compare against the TRMM 0.5° × 0.5° rainfall products, the GCE model domain (i.e., 512 km) was subdivided into eight equal subdomains, each with a horizontal scale of 64 km (comparable to the resolution of the TRMM products). Average rainfall rates and stratiform fractions were then calculated in each subdomain at roughly the same scale as the gridded TRMM products. The average stratiform rain percentage and mean conditional rain rate for each subdomain were then used to bin the data as was done with the PR gridded data. The associated latent, eddy, and radiative heating profiles were also binned using the exact same bins, effectively building the LUT for the new algorithm.

Figure 3 shows the model-simulated probability distribution of rainfall intensity versus stratiform rain percentage over land and ocean regions. The oceanic region was constructed from a combined total of 123 days of model integration from the SCSMEX, TOGA COARE,

TABLE 3. PR-estimated rainfall amount and stratiform % over the global tropics, land, oceans, SCSMEX (1998), SCSMEX (10 yr), ARM (2002), and ARM (10 yr).

	Rainfall amount (mm day^{-1})	Stratiform rain percentage (%)
Global tropics	2.26	52.8
Ocean	2.35	55.0
Land	2.06	47.4
SCSMEX (1998)	11.24	42.3
SCSMEX (10 years)	3.64	49.8
ARM (2002)	2.59	35.7
ARM (10 years)	2.36	41.1

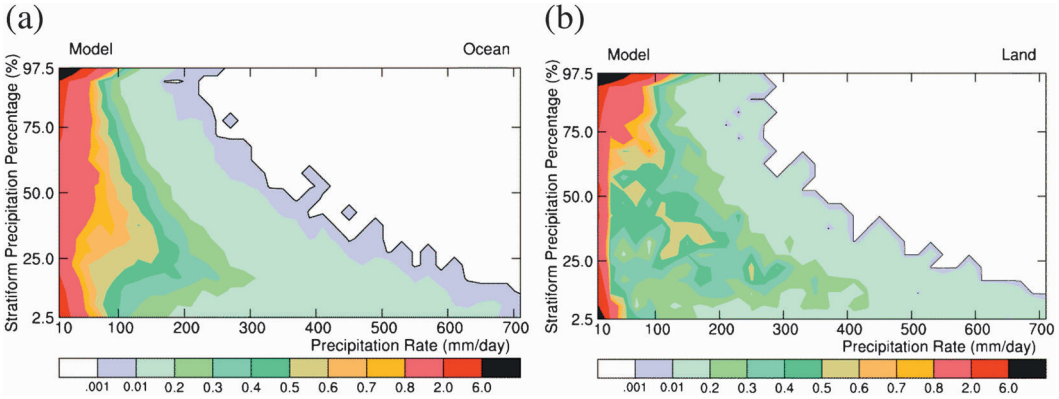

FIG. 3. As in Fig. 2, but for GCE model simulation for (a) oceanic (TOGA COARE, GATE, and SCSMEX) and (b) continental (ARM 1997 and 2002) cases.

and GATE cases. The land region consists of just 49 days of model integration for the two ARM cases. This is why the oceanic distribution is smoother. The model results have overall features that are similar in many ways to the PR observations (Fig. 1). For example, light rain rates (less than 100 mm day^{-1}) tend to dominate the distributions and more so over ocean and at high stratiform fractions. Peak probabilities shift to higher intensities for the most convective portions of the distributions; also, maximum intensities in the tails of the distributions—and hence the overall widths of the distributions—increase monotonically with increasing convective fraction for both land and ocean. The qualitative similarity between the PR and model distributions suggests that information from the model can be mapped to the observations via surface rain intensity and stratiform fraction characteristics (i.e., bins), providing the basis for a new algorithm. However, there are some notable differences between the PR observations and model simulations. The agreement in the predominance of light rain rates holds true for both moderate and high stratiform fractions for oceanic conditions but only for high stratiform conditions for land. At moderate to high convective fractions, the model tends to have more moderate rain, especially over land. Although not especially prominent, the highest probabilities for the model fall into the very lowest rain intensity bin, whereas for the observations, the highest probabilities fall into slightly more intense bins. The reason for this discrepancy is that the minimum detectable return for the PR is 17 dBZ, which is equivalent to about 0.4 mm h^{-1} (or 9.6 mm day^{-1}) of rain. Another difference is that the shift in peak occurrence and extreme values to higher intensities with increasing convective fraction is more pronounced and begins sooner, especially for land conditions, in the model simulations.

Figure 4 shows the relationship between rainfall intensity and stratiform rain percentage for each of the individual land and ocean cases. The two summer land cases, ARM-SGP-97 and -02, are similar to each other, with the moderate to strongly convective parts of their distributions having probabilities that are shifted to significantly higher intensities than the oceanic cases. The oceanic cases are also more similar to each other than they are to either of the land cases. The overall trend between land and ocean is similar between the model and observations with there being an increase in convective fraction and a shift in the distribution to higher intensities at higher convective fractions for land relative to ocean; however, in addition, superimposed on this trend is a general shift from lower to higher rain intensities for the simulated land distributions.

Table 4 shows grid-averaged total rainfall and stratiform rain percentage for each of the GCE simulated cases. The oceanic cases have more rainfall than the continental. This is due primarily to the fact that the oceanic environments have higher precipitable water contents (i.e., more moisture) than the continental (see Table 1 in Tao et al. 2004). The vertically integrated water vapor content for the SCSMEX case is very moist (over 62 g cm^{-2}) compared to the TOGA COARE and GATE cases. That is why the SCSMEX simulation has the largest amount of rainfall. However, although the TOGA COARE environment is moister than that for GATE, it has less rainfall because the model simulation starts in November, which did not have many active convective events. In general, the tropical oceanic cases should have a higher stratiform amount (i.e., 40%–50%) than the midlatitude continental cases. However, the ARM cases also have a large stratiform rain fraction (from 36%–41%) because they include frontal cases. Houze (1977), Zipser et al. (1981), and Gamache and Houze (1983) estimated that widespread stratiform rain accounted for about 32%–49% of the total rainfall during GATE. The fraction of stratiform rainfall from midlatitude squall

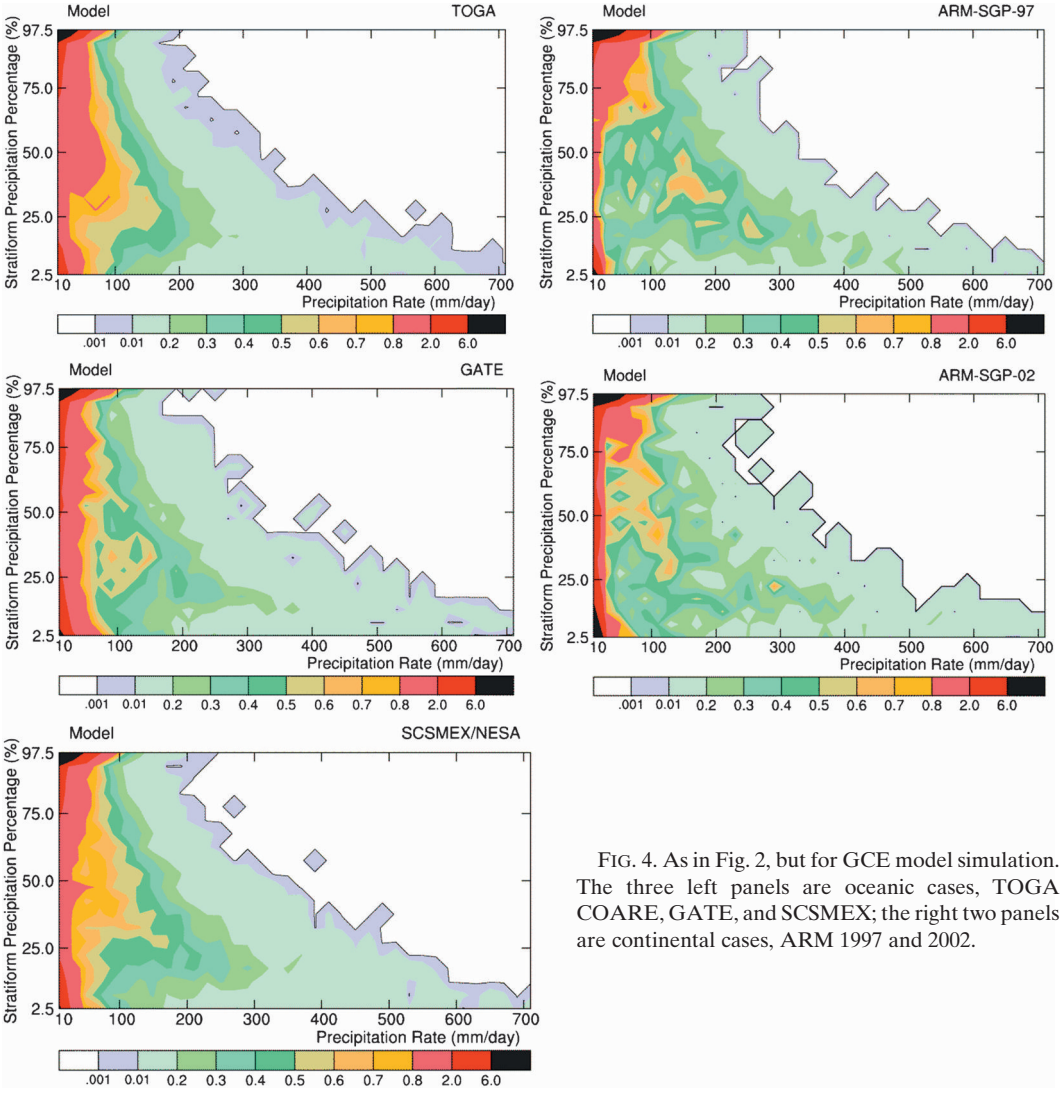

FIG. 4. As in Fig. 2, but for GCE model simulation. The three left panels are oceanic cases, TOGA COARE, GATE, and SCSMEX; the right two panels are continental cases, ARM 1997 and 2002.

lines has been estimated at 29%–43% (Rutledge and Houze 1987; Johnson and Hamilton 1988). The GCE model-simulated results are in good agreement with these observations.

Although the GCE model-simulated stratiform rain percentage for the SCSMEX and ARM-SGP-02 cases are in excellent agreement with the TRMM PR estimates, comparing the GCE model simulations with the PR observations (Table 3) shows that the simulated rainfall amount for the ARM-SGP-02 case is much larger than was estimated by the PR. Sampling may be the reason for this difference as the GCE model-simulated rainfall

TABLE 4. CRM-simulated rainfall amount and stratiform percentage for SCSMEX (1998), ARM (1997, 2002), TOGA COARE (1992), and GATE (1974).

	Simulated rainfall amount (mm day^{-1})	Stratiform rain percentage (%)	Estimated rainfall amount (mm day^{-1})
SCSMEX	12.31	42.6	11.35
ARM (1997)	4.31	41.3	4.32
ARM (2002)	4.85	36.0	4.77
TOGA COARE (1992–93)	7.72	47.6	9.32
GATE (1974)	10.56	41.4	11.38

amounts for the SCSMEX, ARM (1997 and 2002), and GATE cases are in good agreement with those estimated by sounding networks.[6] For the TOGA COARE case, however, the model produced 17% less rainfall than was estimated from the sounding budget. The GCE model was previously used to simulate two TOGA COARE cases, 10–17 December and 19–27 December 1992, and the simulated rainfall was in excellent agreement with the sounding estimates (see Table 5 in Tao et al. 2004). The current difference could be due to the longer model integration. The longer model integration could allow for larger error accumulation. In addition, the longer model integration included less active periods associated with shallow convection that require a finer model grid resolution (e.g., 250 m or finer).

c. GCE model-simulated heating budget components

The apparent heat source Q_1 can be directly related to the contributions by cloud effects, which in turn can be explicitly estimated with the GCE model (Soong and Tao 1980; Tao and Soong 1986; Tao et al. 1993b, and many others):

$$Q_1 = \overline{\pi}\left[-\frac{\partial \overline{\rho} w'\theta'}{\overline{\rho}\partial z} - \nabla \cdot V\theta'\right] + \frac{1}{cp}[L_v(c-e) + L_f(f-m) + L_s(d-s)] + Q_R, \quad (1)$$

where the primes indicate deviations from the large-scale environment mainly due to small-scale cloud processes. The variable θ is potential temperature; ρ is air density; $\overline{\pi} = (p/p_{oo})^{R/c_p}$ is nondimensional pressure (where p and p_{oo} are dimensional and reference pressures, with p_{oo} taken as 1000 hPa); and c_p and R represent the specific heat at constant pressure and the gas constant of dry air, respectively. The variables L_v, L_f, and L_s are the latent heats of condensation, freezing, and sublimation, respectively; the variables c, e, f, m, d, and s respectively denote the microphysical mass transfer rates for condensation of cloud droplets, evaporation of cloud droplets and rain drops, freezing of water droplets and rain drops, and the melting, deposition, and sublimations of ice particles (i.e., crystals, snow flakes, graupel, and hail).

The term $(1/c_p)[L_v(c-e)+L_f(f-m)+L_s(d-s)]$ is the LH due to microphysical phase changes. As defined in Yanai et al. (1973), Q_1 is the apparent heat source, while Q_R is the radiative heating/cooling rate. The first two terms on the right-hand side of Eq. (1) are the vertical and horizontal eddy heat flux convergence—$\overline{\pi}[\overline{\partial w'\theta'/\partial z}]$ and $\overline{\pi}[\overline{\nabla \cdot V'\theta'}]$—where the horizontal eddy term is neglected when Eq. (1) is spatially averaged over a large area suitable for large-scale diagnostic analysis or over the GCE model if a cyclic lateral boundary condition is applied. The horizontal eddy term (entrainment and detrainment) may not be negligible over a small area, such as the GCE model subdomains used in this study.

Figures 5 and 6 show the main components of the simulated heating structures (i.e., latent, eddy, and radiative) derived from composites of the land and oceanic cases, respectively. For each heating component, individual heating profiles are sampled first as a function of rain intensity (i.e., at 0–20, 80–100, 180–200, 380–400 and 480–500 mm day^{-1}) for a given stratiform amount (i.e., 0%–5%, the most convective) and then as a function of stratiform fraction (i.e., 0%–5%, 20%–25%, 45%–50%, 70%–75%, and 95%–100%) for a given rain intensity (i.e., 140–160 mm day^{-1}, approximately the strongest common rain rate among the different stratiform bins). The heating profiles were first summed over the individual GCE model subdomains (i.e., 64 continuous grids with 1-km spacing) and then normalized by the rain area and binned according to the conditional rain rates and stratiform fraction in each subdomain. This approach assumes that all of the LH in each subdomain is associated with the rain area in that subdomain (i.e., LH not in the rain area but still in the subdomain is still included in the average for the rain area). This assumption is also made for the eddy heating but not the radiation, which is also summed over the entire grid box but normalized by the total grid area. Binning is still the same as for the LH. Notable patterns include the following: 1) the magnitude of LH increases with increasing surface rain intensity (Figs. 5a and 6a); 2) the level of maximum heating increases with increasing rain intensity (Figs. 5a and 6a); 3) the depth of heating increases with increasing rain intensity so that light rain is associated with shallow convection and heavy rain with deep convection (Figs. 5a and 6a); 4) both eddy and radiative heating are much smaller than LH but may be nonnegligible for light surface rain rates (i.e., less than 100 mm day^{-1}, Figs. 5b,c,e,f and 6b,c,e,f); and 5) the level of maximum heating increases with increasing stratiform fraction (Figs. 5d and 6d). There are some differences between the land and ocean profiles, namely a double heating maxima in the continental convective profiles for weak rain rates (Fig. 6a), a higher level of maximum heating over land (Figs. 5a and 6a), and stronger eddy heating over land (Figs. 5b and 6b). The latter is due to having stronger convective vertical velocities over land.

These GCE model-simulated heating profiles, which are in many ways in good agreement with observed convective

[6] In addition to the inherent sampling errors, which are likely to be significant, associated with comparing the PR against the relatively small variational analysis domains, the PR did not cover the northern half of the ARM variational analysis domain.

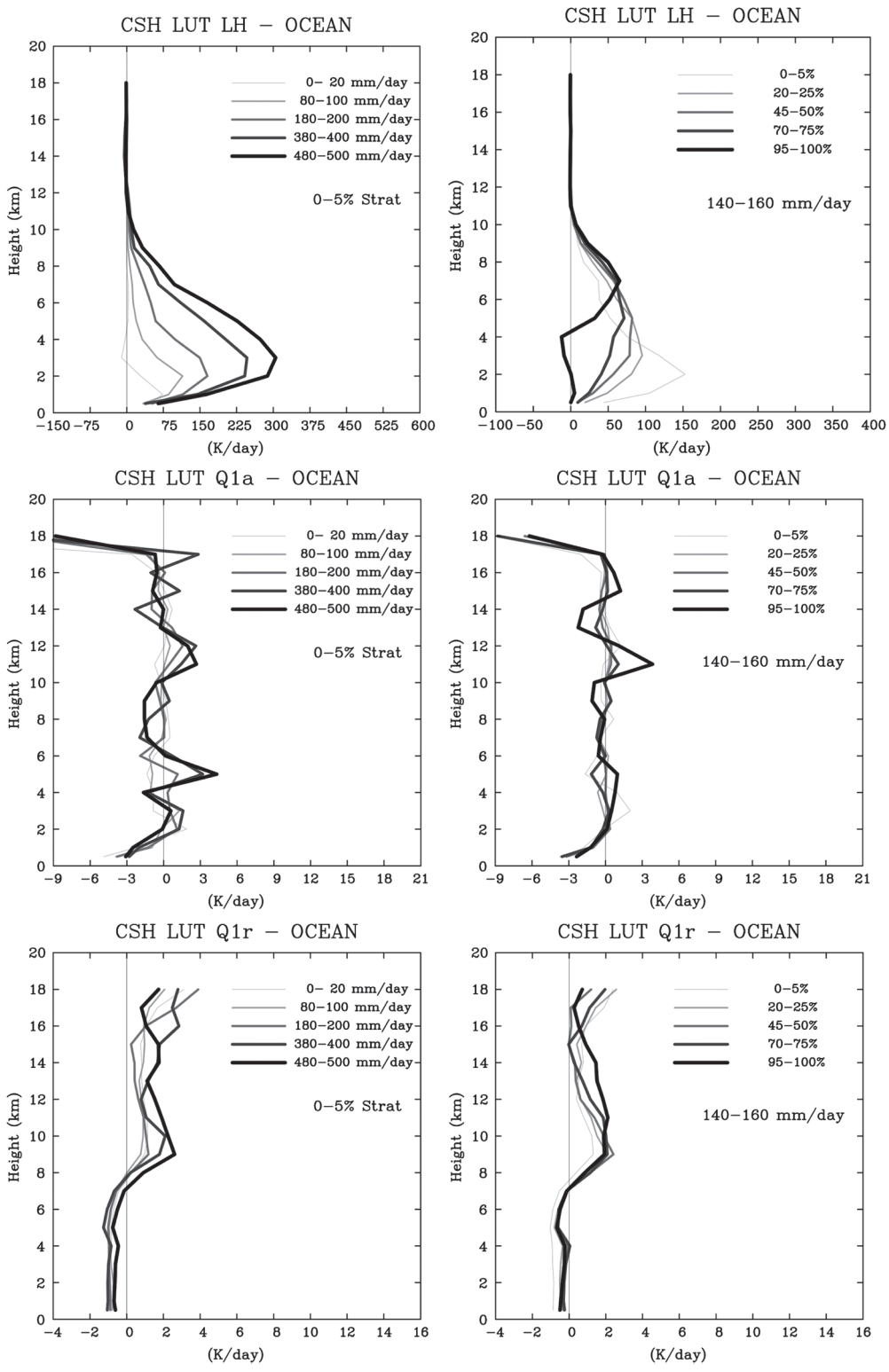

FIG. 5. Mean vertical profiles of (top) latent, (middle) eddy, and (bottom) radiative heating rates for various conditional rain intensity and stratiform fraction bins from the GCE-based oceanic LUT.

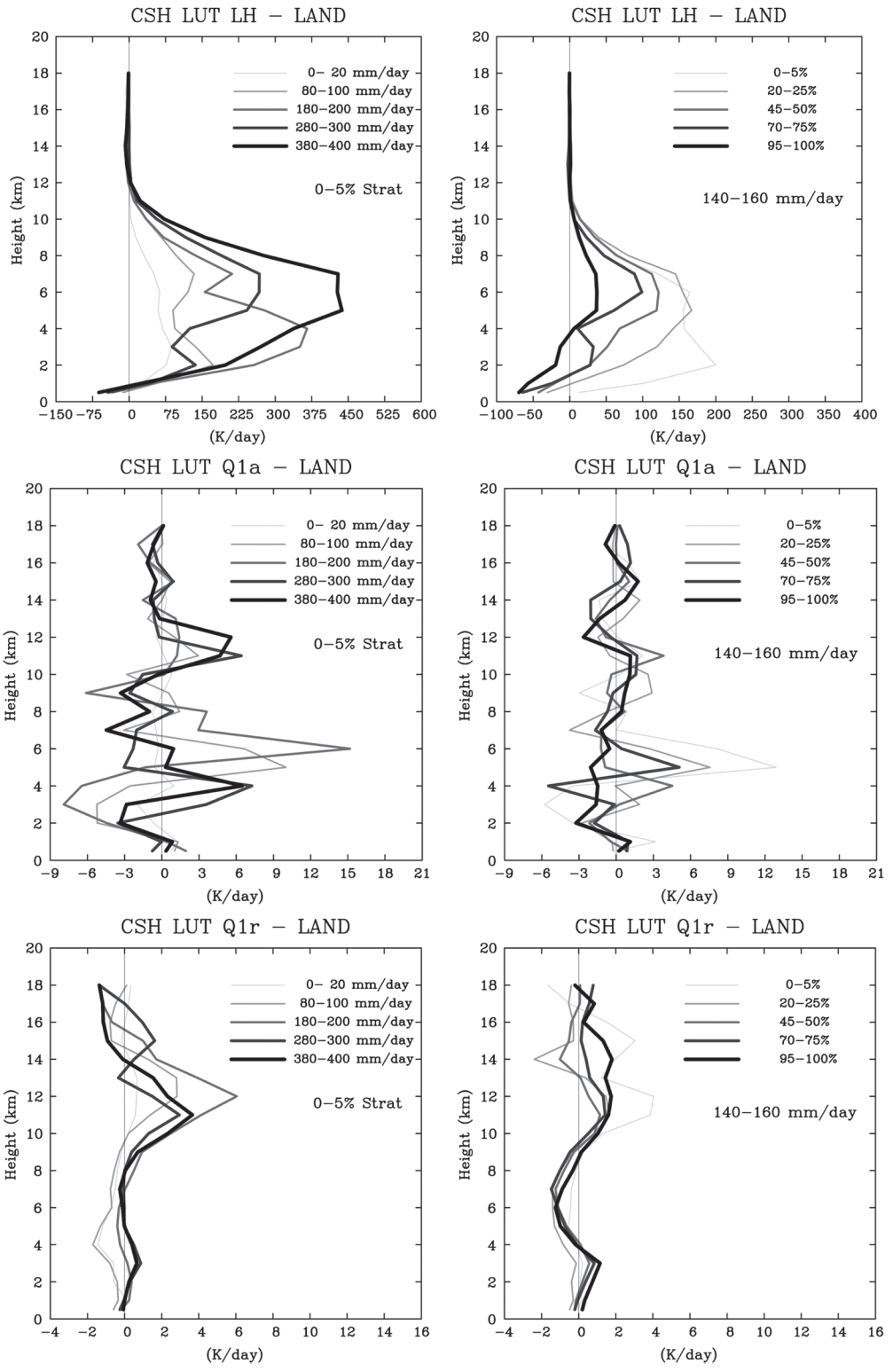

FIG. 6. As in Fig. 5, but for the continental LUT.

and stratiform heating structures (Johnson 1984; Houze 1982, 1997), constitute the new CSH algorithm's LUT.

4. A new CSH algorithm: Details, evaluation, and application

The CSHv1 algorithm (Tao et al. 1993a) uses surface precipitation rates, amount of stratiform rain, and an LUT of rain-normalized convective and stratiform diabatic heating profiles (i.e., Q_1) representing various types of cloud systems of differing geographic origin that were obtained from GCE model simulations and budget calculations. The CSHv1 LUT consists of 20 pairs of heating profiles: 16 oceanic and 4 continental cases. For most applications, those 20 pairs are composited into just two convective/stratiform pairs, representing general ocean and land conditions. A single additional pair is used to represent shallow heating. The new CSH algorithm (hereafter referred to as CSHv2) also uses surface precipitation rates and stratiform rain fraction, but there are several notable differences. The key difference is in the new LUT and how it is accessed. First, there are many more heating profiles (approximately 700 total) in the new LUT because of their being separated into detailed intensity and stratiform bins. And second, the profiles are distributed and thus accessed according to conditional rain rates. Together these lead to several potential advantages regarding heating structure. Obviously, having many more profiles in the LUT allows for the possibility of having many more heating structures. For example, rather than just having shallow or deep heating profiles, the new LUT allows the depth of heating to vary considerably[7] (e.g., Fig. 5a). Using conditional rain rates is what allows those structures to be better differentiated. For example, given a stratiform fraction and an average rain rate over a region (i.e., a $0.5° \times 0.5°$ area), knowing that that average rain rate is due to a small area of intense rain (e.g., a single intense convective cell) rather than a larger area of weak rain (e.g., a broader field of weaker convective cells) allows the algorithm to select a more representative heating structure. In CSHv1, these two rain areas would have been treated the same.

There are also additional refinements in CSHv2. In addition to the LUTs based on grids with rain, an additional set of LUTs is constructed in a like manner but using grids that do not contain rain themselves but are adjacent to grids with rain. Heating in these model subdomains is summed over the entire subdomain as before but then normalized by the average rain area from the surrounding grids and binned according to the average conditional rain rate from the surrounding grids. This allows for heating to be retrieved in areas that are nonraining but that are adjacent to raining areas. Typically the LH in these near rain areas is on the order of or slightly stronger than the eddy term within the rainy areas or about 1–2 orders of magnitude less than the LH in the raining areas. LH profiles next to stratiform areas have weak heating aloft and weak cooling at lower levels (similar to classic stratiform heating profiles but weaker), whereas profiles next to convective areas have weak cooling aloft and weak heating at low levels. The eddy term in the near-rain areas is weaker but on the same order as that in the rainy areas. Radiation, which is averaged over the entire subdomain area as it was for the rainy LUTs, is of the same order of magnitude as the radiation in the rainy areas. Finally, mean latent, eddy, and radiative heating/cooling profiles are constructed from all of the remaining grids (i.e., those which neither have rain nor are adjacent to rain). The LH and eddy heating in these profiles are quite small, but the radiation is comparable to that for the rain and near-rain areas and is thus the dominant term for this region.

Next, the new CSH algorithm is evaluated using a self-consistency approach and then applied to a 10-yr TRMM dataset and compared against the CSHv1 algorithm.

a. Consistency check

The first step in evaluating the new CSHv2 algorithm is to perform a consistency check with CRM data since those data (e.g., the heating profiles and the surface rain characteristics) are internally self consistent. Surface rain data (i.e., conditional and average rain rates and the associated stratiform fraction) were extracted from the long-term SCSMEX simulation every hour for each model subdomain (i.e., 64 km) and supplied to the CSHv2 algorithm, which was then used to reconstruct the heating profiles. The retrieved heating profiles from the algorithm can then be compared against those from the CRM, which can be regarded as the ''truth.'' Both sets of profiles can also be compared to those derived from the diagnostic sounding budget, which was used to force the model. These types of comparisons against observations and CRM simulations have been a standard way to perform consistency checks on algorithms in the past (Tao et al. 1990, 1993a, 2000; Olson et al. 1999, 2006; Shige et al. 2004, 2007, 2008, 2009).

Figure 7 shows the time series of domain-average total heating profiles (i.e., Q_1) from the GCE model simulation, the CSHv2 reconstructed heating profiles using the model surface rain data, and the sounding-based diagnostic heating budget for the SCSMEX case. The CSHv2 heating was reconstructed for all three types of subdomains: rainy, near rain, and away from rain. The results

[7] Mean echo top heights from the PR and from the model correlate nicely over almost the entire range of LUT bins (not shown).

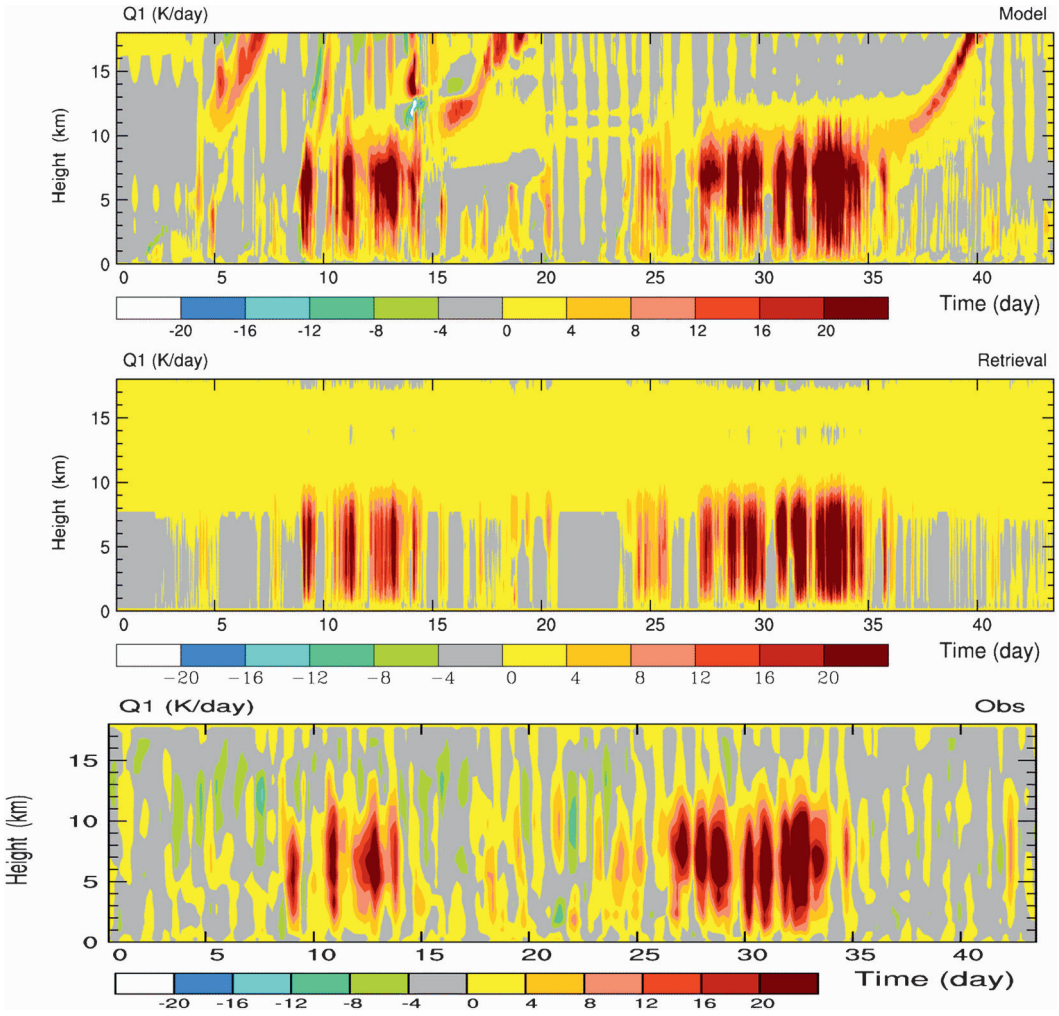

FIG. 7. (top) Modeled, (middle) retrieved, and (bottom) observed time–height cross sections of domain-average Q_1 for SCSMEX NESA.

show that the temporal variation of the CSHv2 heating agrees well with that from the GCE simulation and the sounding budget. Both the model and the retrievals have finer-scale time variations than the budget because they are every hour as opposed to every 6 h. One notable difference is that the retrieved heating structure shows light heating above the 10-km level at all times. This is an artifact of spurious radiative heating in the model simulation being averaged into the CSHv2 ''away from rain'' radiative heating LUT profile. The strong heating and cooling evident in the upper troposphere of the GCE simulation are mainly caused by radiative processes.

Forty-four-day-averaged heating profiles from the model simulation, the CSHv2 reconstructions, and the sounding budget are shown in Fig. 8. These profiles are simply the time averages of the profiles shown in Fig. 7. The time-averaged CSHv2 reconstructed heating profile agrees very well with the model. The level of maximum heating is about 7 km for both the model and the CSHv2 algorithm, which is in good agreement with the sounding budget. Both the simulated and reconstructed heating profiles also have a distinct cooling near 4 km, which is due to the melting processes. This is because the eddy heat flux convergence compensates for this cooling. Both the GCE and CSHv2 average profiles are stronger than that from the sounding budget. This is primarily due to the fact that the model did not simulate the strong cooling in the middle and lower troposphere between active convective events evident in the budget (Fig. 7).

b. Application

The top two panels of Fig. 9 show the 10-yr mean Q_1 at two different altitudes, 1 and 7 km, over the global tropics obtained from the new CSHv2 algorithm using the essentially daily gridded PR rainfall product from 3G68. The concept of the new and old CSH algorithms is

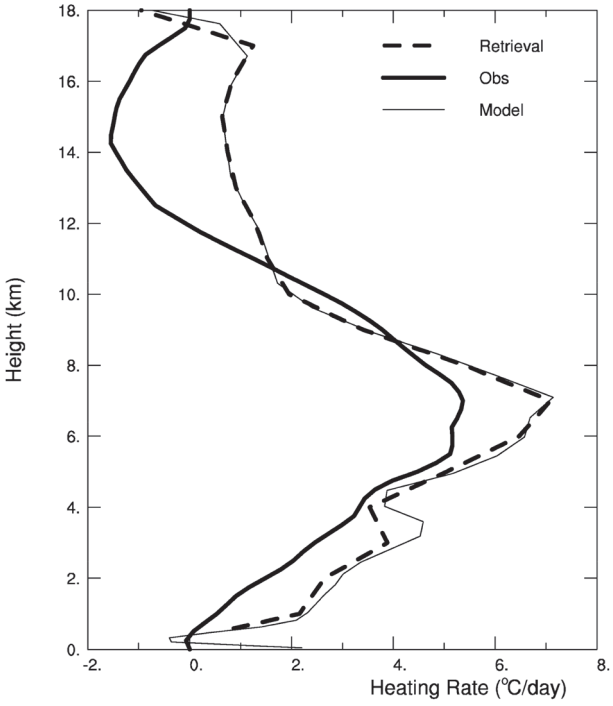

FIG. 8. Observed (thick solid), modeled (thin solid), and retrieved (thick dashed) mean vertical profiles of Q_1 over SCSMEX NESA.

the same. The main difference between the new and old CSH algorithms is the LUT and how it is accessed. However, another useful feature of the new version is that all of the major heating components are now retrieved separately. Thus, for example, to facilitate comparisons with CSHv1, the total heating shown in this section using the 10 yr of PR data include all of the components in grids where it is raining, the LH and eddy components in the near-rain grids (which are a new feature and not something that was intentionally omitted in CSHv1), and none of the components in the ''away from rain'' grids. As expected from the design of the CSH algorithm, the horizontal distribution of the estimated Q_1 structure is similar to the surface rainfall pattern (lower panel in Fig. 9). For example, there are well-defined ITCZs across the Pacific, Atlantic, and eastern Indian Ocean, a well-defined South Pacific convergence zone (SPCZ) in the south-central Pacific Ocean, and midlatitude storm tracks over and downwind of the continents. At the lowest levels in CSHv2, oceanic rain is associated with robust heating, while cooling is prevalent for continental rainfall (Fig. 9, middle panel). At upper levels, heating is intense and stronger over continents than over oceans (Fig. 9, top panel).

To contrast the new version of the CSH algorithm, CSHv2, with the old, CSHv1, cross sections of 10-yr mean zonal average heating were constructed from each algorithm using the same daily gridded PR dataset (note that additional PR echo top height information was used for the CSHv1 algorithm to screen for shallow convection but was not used for CSHv2). The results for CSHv2 and CSHv1 are shown in the top and middle panels of Fig. 10, respectively. Clearly, both versions show two heating maxima. Both of these maxima occur at the same locations and are in response to the surface rainfall associated with the ITCZ (at ~5°N) in the Northern Hemisphere and the SPCZ in the Southern Hemisphere (~2.5°S). The heating is stronger in the Northern Hemisphere because the surface rainfall is larger in the Northern Hemisphere. This difference has implications for the large-scale circulation, which responds to the heating gradient between the Northern and Southern Hemispheres. Although both versions of the CSH algorithm depict the same basic pattern, the overall CSHv2 heating is noticeably stronger, especially in the lower troposphere near the equator. Also, the level of maximum heating is shifted slightly lower in the new version, from approximately 7 km in CSHv1 down to about 6 km in CSHv2.

Figure 10 (bottom panel) shows the mean 10-yr average heating profiles over the global tropics and subtropics (i.e., between 37°N and 37°S) for the old and new versions of the CSH algorithm. The overall shapes are not that dissimilar. Although the level of maximum heating appears to be at a higher level (based on the curvature) in CSHv1 because of its broad heating maximum aloft (the result of compositing a larger variety of cases), the actual level of peak heating near 7 km is the same for both versions. Heating above 8 km is nearly identical, but between 1 and 8 km the CSHv2 heating profile is significantly stronger by nearly a constant amount. This equates to a larger increase in heating in terms of percentage between 1 and 4 km. The average heating over land and ocean is also shown for each algorithm. From these profiles, it is clear that most of the difference comes from land. The oceanic profiles differ by a much smaller degree and mainly below about 4 km where the CSHv2 profile is stronger. There is very little variation in the heating between land and ocean for CSHv1. For CSHv2, average heating is much stronger over land between 2 and 8 km in altitude, while in the lowest levels there is strong average cooling over land but none over oceans. The stronger mid- to upper-level heating over the land is engrained in the LUT (Figs. 6a,c versus Figs. 5a,c) and is likely the consequence of stronger vertical velocities and a greater amount of ice over land. The strong low-level cooling over land is consistent with it having a drier environment and hence more low-level evaporation.

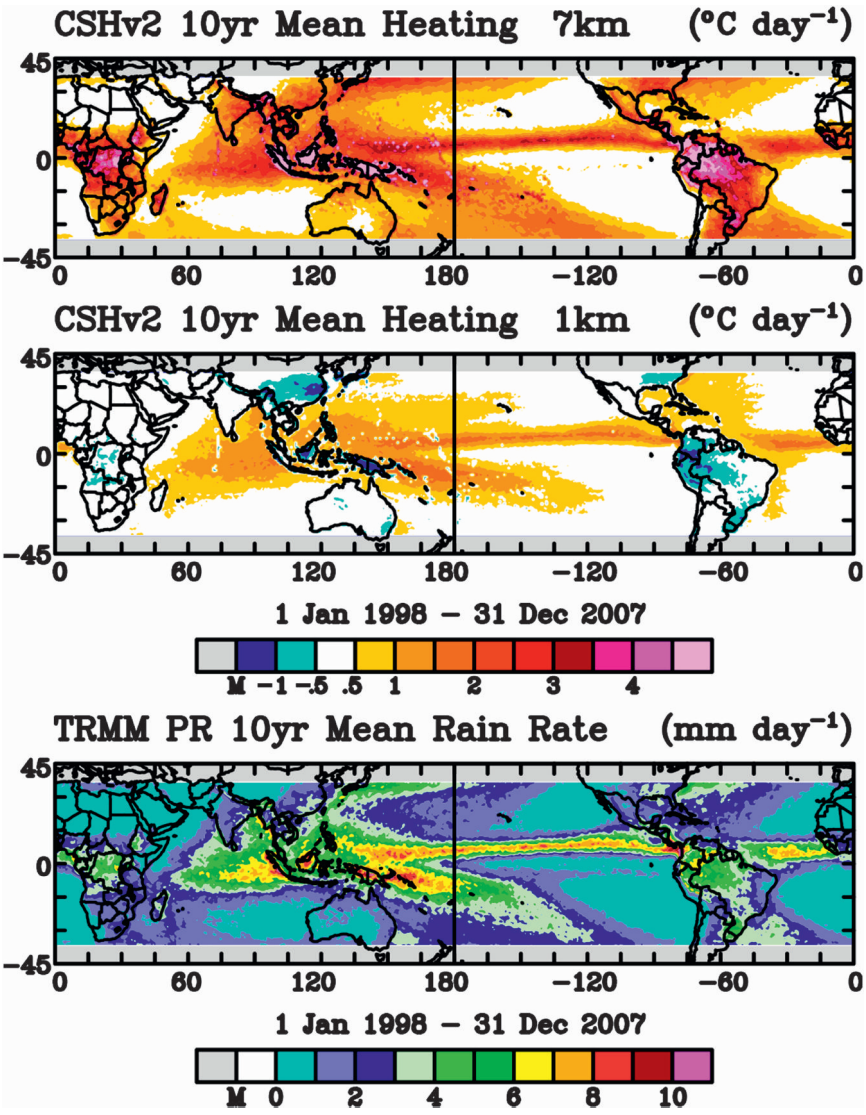

FIG. 9. (top), (middle) Ten-year (1998–2007) mean cloud heating rates over the global tropics at (top) 7 and (middle) 1 km AGL obtained from the new CSH algorithm using (bottom) gridded instantaneous TRMM PR rain rates.

Lin and Johnson (1996) compared the mean Q_1 from the TOGA COARE Marshall Islands region (Yanai et al. 1973) with the GATE region (Thompson et al. 1979). Their results showed that the level of maximum heating was about 6–6.5 km in altitude for the western Pacific (i.e., the TOGA COARE Marshall Islands region) but only about 4 km for the tropical Atlantic (i.e., the GATE region). The lower maximum heating level for the GATE region may be due to the lower SSTs in the eastern Atlantic (Thompson et al. 1979). Greco et al. (1994) calculated Q_1 profiles over South America from a sounding network. Their results indicated that the distribution of heating was quite similar to that obtained from studies of West African squall lines (Chong and Hauser 1990), where peak heating also occurred between 500 and 550 hPa (about 5–6 km). The new CSH algorithm's retrieved level of the maximum heating is about 6 km over land and 7 km over ocean, which is in general agreement with these diagnostic studies. However, the level of the maximum heating has been found to be higher (about 7.5 km) during the monsoon over the South China Sea (SCSMEX NESA; Johnson and Ciesielski 2002) and for convective systems over South America [Large-Scale Biosphere–Atmosphere (LBA); Halverson et al. 2002]. Regional analyses of the new CSH products, including comparisons with diagnostic studies and with other heating products [i.e., products derived from other heating algorithms, such as SLH and

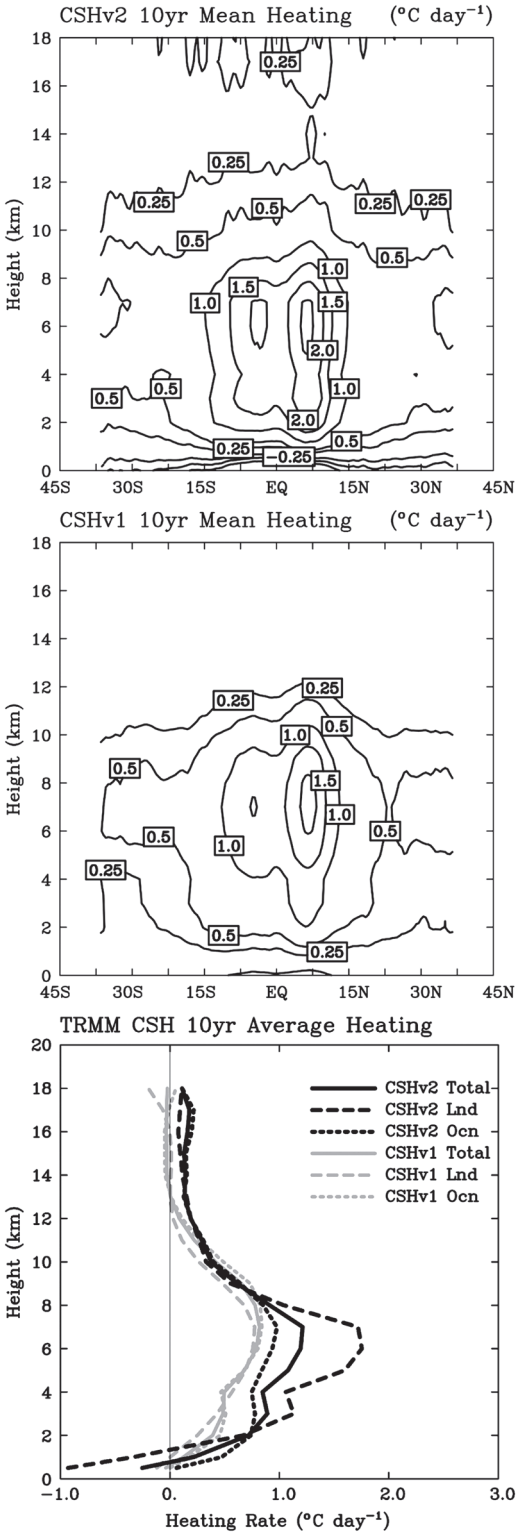

FIG. 10. (top), (middle) Latitude–height cross sections of 10-yr mean zonal cloud heating from the (top) new and (middle) old CSH algorithm; (bottom) 10-yr mean global cloud heating profiles, as well as those for land and ocean, using the new (black) and old (gray) CSH algorithm.

the trained radiometer algorithm (TRAIN)], are still needed.

5. Summary and future work

The relationship between conditional surface rainfall intensity and stratiform fraction over the global tropics and subtropics was examined using both gridded (0.5° × 0.5°) instantaneous TRMM PR observations and long-term (i.e., multiweek) Goddard Cumulus Ensemble (GCE) model simulations sampled over subdomains similar in size to the PR grids. The similarity of the subsequent land and ocean distributions between the satellite observations and model simulations was used to justify the formulation of a new convective–stratiform heating algorithm, CSHv2. LUTs for the new algorithm were obtained by distributing heating/cooling profiles from the model subdomains into the same conditional rain intensity and stratiform rain percentage bins used to construct the surface rainfall distributions. Separate LUTs were constructed for each of the three main heating/cooling components: latent, eddy, and radiative. A similar set of secondary LUTs was created in a like manner for near-rain areas using the mean conditional rain rates and stratiform fractions from neighboring grids. After conducting a self-consistency check using model data, the performance of the new CSH algorithm was presented by comparing its results against those from the previous version of the CSH algorithm, CSHv1, using 10 yr of gridded instantaneous TRMM PR data. The major highlights are as follows:

- Conditional instantaneous surface rain-rate distributions as a function of intensity and stratiform fraction obtained from the model for both land and ocean are similar in many ways to those obtained from PR observations. For example, light rain rates (less than 100 mm day^{-1}) tend to dominate the distributions and more so over ocean and at high stratiform fractions. Peak probabilities shift to higher intensities for the most convective portions of the distributions. Also, maximum intensities in the tails of the distributions and hence the overall widths of the distributions increase monotonically with increasing convective fraction for both the model and the PR over both land and ocean.
- Despite the overall similarity, there are some notable differences between the surface rain distributions from the PR and the model. The agreement in the predominance of light rain rates holds true for both moderate and high stratiform fractions for oceanic conditions but only for high stratiform conditions for land. The model distributions tend to have more moderate rain rates at moderate to high convective fractions, especially over

land. Also, because the minimum detectable return for the PR is 17 dBZ, which is equivalent to about 0.4 mm h^{-1} (or 9.6 mm day^{-1}) of rain, the highest probabilities for the model fall into the very lowest rain intensity bin, whereas for the PR the highest probabilities fall into slightly more intense bins. Finally, for high stratiform fractions, extreme values are stronger in the PR while the converse is true at high convective fractions.

- Of the five cases to which the GCE model was applied, two fell within TRMM satellite coverage. The GCE model-simulated stratiform rain percentage was found to be in excellent agreement with the PR estimates for both the SCSMEX (1998) and ARM (2002) cases; however, the GCE simulated far more rain than the PR observed for the ARM 2002 case. This is likely due to sampling as the GCE simulated rainfall amount is in good agreement with estimates from the sounding budget, from which forcing was used to drive the model.
- LUTs containing the latent, eddy, and radiative heating/cooling profiles for the new CSH algorithm were constructed by compositing the associated model-simulated heating profiles into the same bins used to delineate the surface rain distributions. There were several notable patterns: 1) both the magnitude of LH and the level of maximum heating increase with increasing rain intensity; 2) the depth of heating increases with increasing rain intensity so that light rain is associated with shallow convection and heavy rain with deep convection, allowing the depth of heating to vary without prior knowledge of the echo top heights; 3) eddy and radiative heating are much smaller than LH but may be nonnegligible for light surface rain rates (i.e., less than 100 mm day^{-1}); and 4) the level of maximum heating increases with increasing stratiform fraction. Differences between the land and ocean profiles include a double heating maxima in the continental convective profiles for weak rain rates, a higher level of maximum heating over land, and stronger eddy heating over land.
- Following a successful consistency check of the new CSH algorithm using GCE model data, 10 yr of gridded ''daily'' PR surface rainfall data (i.e., 3G68) were used to derive cloud heating over the global tropics and subtropics with both the new and old versions of the CSH algorithm, CSHv2 and CSHv1, respectively. The overall geographic patterns are quite similar because they are both tied to the same surface rainfall pattern. Mean heating profiles over the global tropics reveal that despite the broad heating maximum aloft for CSHv1, the actual level of peak heating is near 7 km for both versions. Mean heating above 8 km is nearly identical, but between 1 and 8 km the CSHv2 heating profile is significantly stronger by nearly a constant amount. This equates to a larger increase in heating in terms of percentage between 1 and 4 km and shifts the emphasis on heating to lower levels in CSHv2. It is clear from the land and oceanic components that most of the difference comes from land. The oceanic profiles differ by a much smaller degree and mainly below about 4 km, where the CSHv2 profile has stronger low-level heating. While there is little variation in the mean heating over land and ocean for CSHv1, for CSHv2 average heating is much stronger over land between 2 and 8 km in altitude, while in the lowest levels there is strong average cooling over land but not over oceans. These differences are engrained in the LUTs.

The 2D version of the GCE model was used to provide the heating profiles for the new CSH algorithm's LUTs. It is well known that the results from 2D and 3D CRM simulations can differ not only in cloud dynamics but also in microphysics (e.g., Tao and Soong 1986; Johnson et al. 2002; Zeng et al. 2008). More convective cores with stronger vertical velocities exist in a 3D CRM. As a result, the upper tropospheric cloud ice content is higher in a 3D CRM (Zeng et al. 2008). Also, because perturbations in a 2D model are constrained to a vertical plane, there can be more fluctuations in a 2D CRM. The relationship between conditional surface rainfall intensity, its stratiform amount, and the associated heating profiles needs to be examined in 3D.

Finally, only a limited number of CRM-simulated cases were used in this study. Observations from additional field experiments [e.g., the Tropical Warm Pool–International Cloud Experiment (TWP-ICE), the North American Monsoon Experiment (NAME), and the African Monsoon Multidisciplinary Analysis (AMMA)] and a future GPM ground validation (GV) site will be needed to provide new types of initial conditions to the GCE model to expand the number of cases and environments in the LUT. In addition, large-scale analyses from the NASA Goddard Modern Era Retrospective Analysis for Research and Applications (MERRA) could also be used to provide initial conditions and forcing for CRM simulations of environments not sampled by field campaigns. Figure 11 shows some preliminary results using MERRA forcing to drive the GCE model. The fact that the simulation forced by MERRA generally agrees well with that forced by the sounding budget from the field campaign indicates that the GCE+MERRA approach has the potential to provide reasonably good-quality simulations to the CSH algorithm for a variety of locations and conditions, including those regions with large

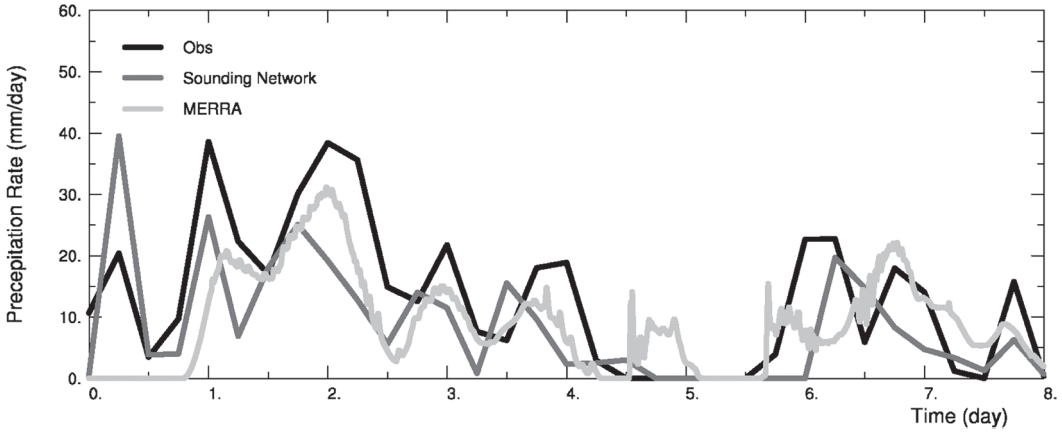

FIG. 11. Eight-day domain average time series of surface rainfall for SCSMEX. The black line is the observed 3-hourly time series from 0600 UTC 18 May to 0600 UTC 26 May 1998. The dark gray line is the 3-hourly time series from the GCE simulation driven by the SCSMEX sounding-based observed large-scale tendencies. The light gray line is same as the dark gray line except that the GCE was driven by tendencies from MERRA output. The two simulations generally agree well with each other and show the viability of using GCE+MERRA to obtain quality simulations for undersampled environments.

surface rainfall, such as the Indian Ocean, SPCZ, South America, and Africa.

Acknowledgments. This research was supported by the NASA Headquarters Atmospheric Dynamics and Thermodynamics Program and the NASA Precipitation Measuring Mission (PMM). The authors are grateful to Dr. R. Kakar at NASA headquarters for his support of this research. We also thank two anonymous reviewers for their constructive comments and suggestions that improved this paper significantly. Acknowledgment is also made to the NASA Goddard Space Flight Center and NASA Ames computing centers for the computational resources used in this research.

REFERENCES

Chong, M., and D. Hauser, 1990: A tropical squall line observed during the COPT 81 experiment in West Africa. Part III: Heat and moisture budgets. *Mon. Wea. Rev.,* **118,** 1696–1706.

Ciesielski, P. E., and R. H. Johnson, 2006: Contrasting characteristics of convection over the Northern and Southern South China Sea during SCSMEX. *Mon. Wea. Rev.,* **134,** 1041–1062.

——, ——, P. T. Haertel, and J. Wang, 2003: Corrected TOGA COARE sounding humidity data: Impact on diagnosed properties of convection and climate over the warm pool. *J. Climate,* **16,** 2370–2384.

Das, S., D. Johnson, and W.-K. Tao, 1999: Single-column and cloud ensemble model simulations of TOGA COARE convective systems. *J. Meteor. Soc. Japan,* **77,** 803–826.

Gamache, J. F., and R. A. Houze Jr., 1983: Water budget of a mesoscale convective system in the tropics. *J. Atmos. Sci.,* **40,** 1835–1850.

Greco, S., J. Scala, J. Halverson, H. L. Massie, W.-K. Tao, and M. Garstang, 1994: Amazon coastal squall lines. Part II: Heat and moisture transports. *Mon. Wea. Rev.,* **122,** 623–635.

Grecu, M., and W. S. Olson, 2006: Bayesian estimation of precipitation from satellite passive microwave observations using combined radar–radiometer retrievals. *J. Appl. Meteor. Climatol.,* **45,** 416–433.

——, ——, C.-L. Shie, T. L'Ecuyer, and W.-K. Tao, 2009: Combining satellite microwave radiometer and radar observations to estimate atmospheric latent heating profiles. *J. Climate,* **22,** 6356–6376.

Halverson, J. B., T. Rickenbach, B. Roy, H. Pierce, and E. Williams, 2002: Environmental characteristics of convective systems during TRMM-LBA. *Mon. Wea. Rev.,* **130,** 1493–1509.

Houze, R. A., Jr., 1977: Structure and dynamics of a tropical squall-line system. *Mon. Wea. Rev.,* **105,** 1540–1567.

——, 1982: Cloud clusters and large-scale vertical motions in the tropics. *J. Meteor. Soc. Japan,* **60,** 396–410.

——, 1997: Stratiform precipitation in regions of convection: A meteorological paradox. *Bull. Amer. Meteor. Soc.,* **78,** 2179–2196.

Johnson, D. E., W.-K. Tao, J. Simpson, and C.-H. Sui, 2002: A study of the response of deep tropical clouds to large-scale thermodynamic forcing. Part I: Modeling strategies and simulations of TOGA COARE convective systems. *J. Atmos. Sci.,* **59,** 3492–3518.

Johnson, R. H., 1984: Partitioning tropical heat and moisture budgets into cumulus and mesoscale components: Implications for cumulus parameterization. *Mon. Wea. Rev.,* **112,** 1590–1601.

——, and P. J. Hamilton, 1988: The relationship of surface pressure features to the precipitation and airflow structure of an intense midlatitude squall line. *Mon. Wea. Rev.,* **116,** 1444–1473.

——, and P. E. Ciesielski, 2002: Characteristics of the 1998 summer monsoon onset over the northern South China Sea. *J. Meteor. Soc. Japan,* **80,** 561–578.

——, S. L. Aves, and P. E. Ciesielski, 2005: Organization of oceanic convection during the onset of the 1998 East Asian summer monsoon. *Mon. Wea. Rev.,* **133,** 131–148.

Klemp, J. B., and R. B. Wilhelmson, 1978: The simulation of three-dimensional convective storm dynamics. *J. Atmos. Sci.,* **35,** 1070–1096.

Lang, S., W.-K. Tao, J. Simpson, and B. Ferrier, 2003: Modeling of convective-stratiform precipitation processes: Sensitivity to partitioning methods. *J. Appl. Meteor.,* **42,** 505–527.

——, ——, R. Cifelli, W. Olson, J. Halverson, S. Rutledge, and J. Simpson, 2007: Improving simulations of convective systems from TRMM LBA: Easterly and westerly regimes. *J. Atmos. Sci.,* **64,** 1141–1164.

Li, X., C.-H. Sui, K.-M. Lau, and M.-D. Chou, 1999: Large-scale forcing and cloud-radiation interaction in the tropical deep convective regime. *J. Atmos. Sci.,* **56,** 3028–3042.

——, ——, and ——, 2002: Dominant cloud microphysical processes in a tropical oceanic convective system: A 2D cloud resolving modeling study. *Mon. Wea. Rev.,* **130,** 2481–2491.

Lin, X., and R. H. Johnson, 1996: Heating, moistening, and rainfall over the western Pacific during TOGA COARE. *J. Atmos. Sci.,* **53,** 3367–3383.

Olson, W. S., C. D. Kummerow, Y. Hong, and W.-K. Tao, 1999: Atmospheric latent heating distributions in the tropics derived from passive microwave radiometer measurements. *J. Appl. Meteor.,* **38,** 633–664.

——, and Coauthors, 2006: Precipitation and latent heating distributions from satellite passive microwave radiometry Part I: Method and uncertainties. *J. Appl. Meteor. Climatol.,* **45,** 702–720.

Rutledge, S. A., and R. A. Houze Jr., 1987: A diagnostic modeling study of the trailing stratiform of a midlatitude squall line. *J. Atmos. Sci.,* **44,** 2640–2656.

Satoh, S., and A. Noda, 2001: Retrieval of latent heating profiles from TRMM radar data. *Proc. 30th Int. Conf. on Radar Meteorology,* Munich, Germany, Amer. Meteor. Soc., 6.3. [Available online at http://ams.confex.com/ams/30radar/techprogram/paper_21763.htm.]

Schumacher, C., and R. A. Houze Jr., 2003: Stratiform rain in the tropics as seen by the TRMM Precipitation Radar. *J. Climate,* **16,** 1739–1756.

Shige, S., Y. N. Takayabu, W.-K. Tao, and D. E. Johnson, 2004: Spectral retrieval of latent heating profiles from TRMM PR data. Part I: Development of a model-based algorithm. *J. Appl. Meteor.,* **43,** 1095–1113.

——, ——, ——, and C.-L. Shie, 2007: Spectral retrieval of latent heating profiles from TRMM PR data. Part II: Algorithm improvement and heating estimates over tropical ocean regions. *J. Appl. Meteor.,* **46,** 1098–1124.

——, ——, and ——, 2008: Spectral retrieval of latent heating profiles from TRMM PR data. Part III: Estimating apparent moisture sink profiles over tropical oceans. *J. Appl. Meteor. Climatol.,* **47,** 620–640.

——, ——, S. Kida, W.-K. Tao, X. Zeng, C. Yokoyama, and T. L'Ecuyer, 2009: Spectral retrieval of latent heating profiles from TRMM PR data. Part IV: Comparisons of lookup tables from two- and three-dimensional simulations. *J. Climate,* **22,** 5577–5594.

Simpson, J., and W.-K. Tao, 1993: The Goddard Cumulus Ensemble Model. Part II: Applications for studying cloud precipitating processes and for NASA TRMM. *Terr. Atmos. Ocean. Sci.,* **4,** 73–116.

Smith, E. A., X. Xiang, A. Mugnai, and G. J. Tripoli, 1994: Design of an inversion-based precipitation profile retrieval algorithm using an explicit cloud model for initial guess microphysics. *Meteor. Atmos. Phys.,* **54,** 53–78.

Soong, S.-T., and Y. Ogura, 1980: Response of trade wind cumuli to large-scale processes. *J. Atmos. Sci.,* **37,** 2035–2050.

——, and W.-K. Tao, 1980: Response of deep tropical cumulus clouds to mesoscale processes. *J. Atmos. Sci.,* **37,** 2016–2034.

Starr, D. O'C., and S. K. Cox, 1985: Cirrus clouds. Part I: A cirrus cloud model. *J. Atmos. Sci.,* **42,** 2663–2681.

Sui, C.-H., and M. Yanai, 1986: Cumulus ensemble effects on the large-scale vorticity and momentum fields of GATE. Part I: Observational evidence. *J. Atmos. Sci.,* **43,** 1618–1642.

Tao, W.-K., 2003: Goddard Cumulus Ensemble (GCE) model: Application for understanding precipitation processes. *Cloud Systems, Hurricanes, and the Tropical Rainfall Measuring Mission (TRMM): A Tribute to Dr. Joanne Simpson, Meteor. Monogr.,* No. 51, Amer. Meteor. Soc., 107–138.

——, and S.-T. Soong, 1986: A study of the response of deep tropical clouds to mesoscale processes: Three-dimensional numerical experiments. *J. Atmos. Sci.,* **43,** 2653–2676.

——, and J. Simpson, 1993: The Goddard Cumulus Ensemble model. Part I: Model description. *Terr. Atmos. Ocean. Sci.,* **4,** 19–54.

——, ——, and S.-T. Soong, 1987: Statistical properties of a cloud ensemble: A numerical study. *J. Atmos. Sci.,* **44,** 3175–3187.

——, ——, S. Lang, M. McCumber, R. Adler, and R. Penc, 1990: An algorithm to estimate the heating budget from vertical hydrometeor profiles. *J. Appl. Meteor.,* **29,** 1232–1244.

——, ——, and S.-T. Soong, 1991: Numerical simulation of a subtropical squall line over Taiwan Strait. *Mon. Wea. Rev.,* **119,** 2699–2723.

——, S. Lang, J. Simpson, and R. Adler, 1993a: Retrieval algorithms for estimating the vertical profiles of latent heat release: Their applications for TRMM. *J. Meteor. Soc. Japan,* **71,** 685–700.

——, J. Simpson, C.-H. Sui, B. Ferrier, S. Lang, J. Scala, M.-D. Chou, and K. Pickering, 1993b: Heating, moisture, and water budgets of tropical and midlatitude squall lines: Comparisons and sensitivity to longwave radiation. *J. Atmos. Sci.,* **50,** 673–690.

——, S. Lang, J. Simpson, C.-H. Sui, B. Ferrier, and M.-D. Chou, 1996: Mechanisms of cloud–radiation interaction in the tropics and midlatitudes. *J. Atmos. Sci.,* **53,** 2624–2651.

——, ——, ——, W. S. Olson, D. Johnson, B. Ferrier, C. Kummerow, and R. Adler, 2000: Vertical profiles of latent heat release and their retrieval for TOGA COARE convective systems using a cloud resolving model, SSM/I, and shipborne radar data. *J. Meteor. Soc. Japan,* **78,** 333–355.

——, and Coauthors, 2001: Retrieved vertical profiles of latent heating release using TRMM rainfall products for February 1998. *J. Appl. Meteor.,* **40,** 957–982.

——, and Coauthors, 2003a: Microphysics, radiation and surface processes in the Goddard Cumulus Ensemble (GEC) model. *Meteor. Atmos. Phys.,* **82,** 97–137.

——, C.-L. Shie, J. Simpson, S. Braun, R. Johnson, and P. E. Ciesielski, 2003b: Convective systems over the South China Sea: Cloud-resolving model simulations. *J. Atmos. Sci.,* **60,** 2929–2956.

——, D. Johnson, C.-L. Shie, and J. Simpson, 2004: The atmospheric energy budget and large-scale precipitation efficiency of convective systems during TOGA COARE, GATE, SCSMEX and ARM: Cloud-resolving model simulations. *J. Atmos. Sci.,* **61,** 2405–2423.

——, and Coauthors, 2006: Retrieval of latent heating from TRMM measurements. *Bull. Amer. Meteor. Soc.,* **87,** 1555–1572.

——, R. Houze Jr., and E. Smith, 2007: The fourth TRMM latent heating workshop. *Bull. Amer. Meteor. Soc.,* **88,** 1255–1259.

Thompson, R. M., Jr., S. W. Payne, E. E. Recker, and R. J. Reed, 1979: Structure and properties of synoptic-scale wave disturbances in the intertropical convergence zone of the eastern Atlantic. *J. Atmos. Sci.,* **36,** 53–72.

Wang, Y., W.-K. Tao, and J. Simpson, 1996: The impact of ocean surface fluxes on a TOGA COARE convective system. *Mon. Wea. Rev.,* **124,** 2753–2763.

Xu, K.-M., and Coauthors, 2002: Intercomparison of cloud-resolving models with the Atmospheric Radiation Measurement summer 1997 intensive observation period data. *Quart. J. Roy. Meteor. Soc.,* **128,** 593–624.

Yanai, M., S. Esbensen, and J. Chu, 1973: Determination of average bulk properties of tropical cloud clusters from large-scale heat and moisture budgets. *J. Atmos. Sci.,* **30,** 611–627.

Yang, S., and E. A. Smith, 1999: Four-dimensional structure of monthly latent heating derived from SSM/I satellite measurements. *J. Climate,* **12,** 1016–1037.

——, W. S. Olson, J.-J. Wang, T. L. Bell, E. A. Smith, and C. D. Kummerow, 2006: Precipitation and latent heating distributions from satellite passive microwave radiometry. Part II: Evaluation of estimates using independent data. *J. Appl. Meteor.,* **45,** 721–739.

Zeng, X., and Coauthors, 2007: Evaluating clouds in long-term cloud-resolving model simulations with observational data. *J. Atmos. Sci.,* **64,** 4153–4177.

——, W.-K. Tao, S. Lang, A. Hou, M. Zhang, and J. Simpson, 2008: On the sensitivity of atmospheric ensembles to cloud microphysics in long-term cloud-resolving model simulations. *J. Meteor. Soc. Japan,* **86A,** 45–65.

——, and Coauthors, 2009: A contribution by ice nuclei to global warming. *Quart. J. Roy. Meteor. Soc.,* **135,** 1614–1629.

Zhang, M. H., and J. L. Lin, 1997: Constrained variational analysis of sounding data based on column-integrated budgets of mass, heat, moisture, and momentum: Approach and application to ARM measurements. *J. Atmos. Sci.,* **54,** 1503–1524.

——, ——, R. T. Cederwall, J. J. Yio, and S. C. Xie, 2001: Objective analysis of ARM IOP Data: Method and sensitivity. *Mon. Wea. Rev.,* **129,** 295–311.

Zipser, E. J., R. J. Meitin, and M. A. LeMone, 1981: Mesoscale motion fields associated with a slowly moving GATE convective band. *J. Atmos. Sci.,* **38,** 1725–1750.